 doi:10.20944/preprints202205.0400.v1

Effects of Pulsatile Flow Rate and Shunt Ratio in Bifurcated Distal Arteries on Hemodynamic Characteristics Involved in Two Patient-Specific Internal Carotid Artery Sidewall Aneurysms: A Numerical Study

Hang Yi[1,*], Mark Johnson[1], Luke Bramlage[2], Bryan Ludwig[2,3], Zifeng Yang[1,**]

[1] Department of Mechanical and Materials Engineering, Wright State University, Dayton, OH 45435, USA

[2] Department of Neurology – Division of NeuroInterventional Surgery Wright State University / Premier Health – Clinical Neuroscience Institute, 30E. Apple St, Dayton, OH 45409, USA

[3] Boonshoft School of Medicine, Wright State University, Dayton, OH 45435, USA

[*] Corresponding Author 1:
Address: 209 Russ Engineering Center, Wright State University, 3640 Colonel Glenn Hwy., Dayton, OH 45435, USA
Phone: (405)7623057
Email: hang.yi@wright.edu

[**] Corresponding Author 2:
Address: 209 Russ Engineering Center, Wright State University, 3640 Colonel Glenn Hwy., Dayton, OH 45435, USA
Phone: (513)331-3070
Email: zifeng.yang@wright.edu

 doi:10.20944/preprints202205.0400.v1

ABSTRACT

The pulsatile flow rate (PFR) in the cerebral artery system and shunt ratios in bifurcated arteries are two patient-specific parameters which may affect the hemodynamic characteristics on the pathobiology of cerebral aneurysms (CAs). Accordingly, a systematic study was employed to investigate the effects of the two parameters on hemodynamic characteristics in two internal carotid artery sidewall aneurysms (i.e., ICASA-1 and ICASA-2) models. Numerical results indicate larger PFRs can cause higher WSS in some local regions of the aneurysmal dome that may increase the probability of small/secondary aneurysms generation than under smaller PFRs. The low WSS and relatively high oscillatory shear index (OSI) could appear under a smaller PFR, which has the potential to cause aneurysmal sac growth and rupture. However, the variances in PFRs and bifurcated shunt ratios have rare impacts on the time-average pressure distributions on the aneurysmal sac, although a higher PFR can contribute more to the pressure increase in ICASA-1 dome due to the relatively stronger impingement by the redirected blood stream than in ICASA-2. Simulation results also present the variances of shunt ratios have rare impacts on the hemodynamic characteristics in sacs, mainly because the bifurcated location is not close enough to the sac in present models. Furthermore, it has been found that the vortex location plays a major role in the temporal and spatial distribution of the WSS on the luminal wall, varying significantly with the cardiac period.

KEYWORDS: Internal carotid artery sidewall aneurysm (ICASA); hemodynamic behaviors; computational fluid dynamics (CFD); pulsatile flow rate (PFR); bifurcated shunt ratio; wall shear stress (WSS); oscillatory shear index (OSI), time-averaged pressure (TAP).

 doi:10.20944/preprints202205.0400.v1

1. INTRODUCTION

Intracranial arterial walls have the probability to generate cerebral aneurysms (CAs) by aberrant focal dilatations [1-4], which may lead to unexpected consequences (e.g., stroke, coma and/or death) in case that the aneurysmal dome ruptures [5-8]. Indeed, it has been estimated that 90% of spontaneous subarachnoid hemorrhages (SAHs) can be attributed to the rupture of cerebral aneurysms, which range in sizes from less than 5 mm to more than 25 mm patient-specifically [9, 10]. This lack of clear guidance to evaluate unruptured CAs may lead to a false sense of security when withholding aneurysm treatment in an aneurysm misidentified as benign, or an unnecessary repair of more benign aneurysms which are misidentified as high risk for rupture. Not all patients with unruptured, cerebral aneurysms are necessary to treat surgically, and treatment has been a matter of debate for many decades [10-12]. Thus, a comprehensive understanding of the pathophysiology of CAs is extremely important for physicians to evaluate treatments more responsibly. Specifically, hemodynamic characteristics, i.e., flow patterns, wall shear stress (WSS), oscillatory shear index (OSI), and time averaged pressure (TAP), playing an important role in the formation, growth, and rupture of cerebral aneurysms, should be identified precisely using qualitative and quantitative manners [13-17]. So far, the risks associated with various factors (i.e., aneurysmal dome locations, high risk aneurysmal morphologies, pre- and post-treatment states, and arterial blood flow conditions) on the pathophysiology of CAs have been estimated, to some extent, using different research strategies (i.e., *in vivo*, *in vitro*, and *in silico*), which were summarized by previous efforts [18-25]. Nevertheless, the pulsatile flow rates are typically patient-specific [26, 27], and many studies had tentative investigations on how the varying pulsatile blood flowrates/pressures will influence hemodynamic characteristics (i.e., WSS and OSI) in cerebral arteries or CAs [28-33]. Sekhame and Mansour [28] studied time averaged WSS distributions in internal carotid artery (ICA) rather than in CA with three pulsatile flow rates using COMSOL Multiphysics (COMSOL Inc., Stockholm, Sweden), and found waveform boundary conditions have important effects on the overall instantaneous hemodynamic factors assessed on the geometries while time averaged WSS was constant for the studied cases. Sarrami-Foroushani et al. [29] studied the hemodynamic patterns in a ruptured ICA aneurysm with varying flow waveforms, and discovered that systolic and time-averaged WSS and pressure on the aneurysm wall showed a proportional evolution with the mainstream flow rate. However, some of above-mentioned studies reconstructed the models based on the image scanned from a ruptured aneurysm, which could be extremely different from the morphology of the realistic aneurysm. Also, the mesh independence test in the simulations was not investigated which may lead to significant differences in the results among different research groups despite similar geometries, boundary conditions, and blood properties. More importantly, another two parameters, i.e., the detailed flow field (i.e., velocity gradient) in the aneurysmal lumen, and the variations of shunt ratios in bifurcated distal arteries with the simultaneously varied inlet flowrates have not been investigated in previous studies. Moreover, since the cerebral aneurysm is always morphologically patient-specific, more investigations are still needed to enrich the intracranial aneurysm research community to better understand the pathophysiology in CAs. Comparing to the experiments involving *in vivo* and *in vitro*, the computational fluid dynamics (CFD) based *in-silico* methods adopt an accessible and noninvasive manner to predict the blood flow patterns in CAs. Specifically, numerical modeling employs physiologically based reconstructed models and initial/boundary conditions which can aid in identifying major translational knowledge gaps as well as provide a platform for implementing and evaluating

Preprints (www.preprints.org) | NOT PEER-REVIEWED | Posted: 30 May 2022 doi:10.20944/preprints202205.0400.v1

potential solutions [14, 20, 34-43]. This approach offers several advantages, including the ability to: (1) study a system or phenomenon at different spatial and temporal scales in the aneurysmal sac, (2) perform analysis under varied conditions, i.e., patient-specific blood flow conditions and arterial geometries, (3) evaluate critical situations in a noninvasive way, and (4) carry out cost-effective high-fidelity studies which can accelerate the better understanding of hemodynamic factors affecting the generation, growth and rupture of the cerebral aneurysmal domes than *in vivo*/*in vitro*.

The objectives of this study are to use CFD methods to quantify the effects of pulsatile flow rate and shunt ratios in bifurcated arteries on the hemodynamic characteristics in two patient-specific internal carotid artery sidewall aneurysm (ICASA) models (e.g., ICASA-1 and ICASA-2). Specifically, a systematically parametric study was employed to study the effects of pulsatile flow rate, shunt ratios in bifurcated distal arteries, and transient cardiac pulsatile flow on hemodynamic transport behaviors in ICSASA-1 and ICSASA-2 models. The novel results obtained in this study can contribute to the intracranial aneurysm community's knowledge about how blood flow patterns in the aneurysmal sac can be affected by different patient-specific pulsatile flow rates and shunt ratios in bifurcated distal arteries.

2. NUMERICAL METHODOLOGY

2.1. Geometry and Mesh

To study the hemodynamic characteristics in ICASA models, two patient-specific cerebral aneurysm models (see **Figs. 1**), i.e., (a) ICASA-1 (73-year-old, female), and (b) ICASA-2 (35-year-old, female), were built based on data provided by Miami Valley Hospital (Dayton, Ohio, USA) [44, 45]. In ICASA-1 model, the blood flows in through the ICA and flows out from the bifurcated distal arteries, i.e., posterior communicating artery (PComA) and ICA distal. In ICASA-2 model, the blood flows in through the ICA to its distal bifurcation, i.e., middle cerebral artery (MCA) and anterior cerebral artery (ACA). In this study, the ICA distal and MCA are denoted by A1, and PComA and ACA are denoted by A2 (see **Fig. 1**), respectively, for simplicity.

Two sets of poly-hexcore meshes have been generated for each aneurysm model using ANSYS Fluent Meshing 2021 R2 (Ansys Inc., Canonsburg, PA), with different mesh sizes for the mesh independence test. Mesh details for the ICASA-1 and ICASA-2 models are shown in **Table 1** and **Fig. 1**. Regions (i.e., aneurysm sac) with more possible rupture risks were discretized with refined mesh elements. Mesh independence tests were investigated by the comparisons of nondimensionalized velocity profiles $V^*_{i-i'}$ at selected lines (see **Fig. 2**), i.e., AA' and BB', in the two ICASA models, respectively, with a constant blood flow rate of 1.5 ml/s, density of 1050 kg/m^3, and viscosity of 3.5e-3 kg/m-s. Moreover, the WSS magnitudes on the edge of selected planes, i.e., plane A-A' and plane B-B', were compared in the generated meshes, with the corresponded ICASA models to obtain the final mesh for the parametric studies (see **Fig. 2**). The equations for nondimensionalized velocity $V^*_{i-i'}$ and nondimensionalized length, i.e., $L^*_{i-i'}$ and $L^*_{i''-i''}$, can be expressed by:

$$V^*_{i-i'} = \frac{|V|}{|V_{in}|} \tag{1}$$

$$L^*_{i-i'} = \frac{l'}{L_{ii'}} \tag{2}$$

Preprints (www.preprints.org) | NOT PEER-REVIEWED | Posted: 30 May 2022 doi:10.20944/preprints202205.0400.v1

$$L^*_{i''-i''} = \frac{l''}{L_{i''i''}} \tag{3}$$

where V_{in} is the inlet velocity, and V is the velocity for the selected lines $A \rightarrow A'$ and $B \rightarrow B'$ for the two ICASA models, respectively. l denotes the length of lines AA' and BB' from $A \rightarrow A'$ and $B \rightarrow B'$, separately. l'' is the arc length from point $A'' \rightarrow A''$ and $B'' \rightarrow B''$, respectively. In addition, $L_{i''i''}$ represents the perimeter of the arcs $A''A''$ and $B''B''$, separately.

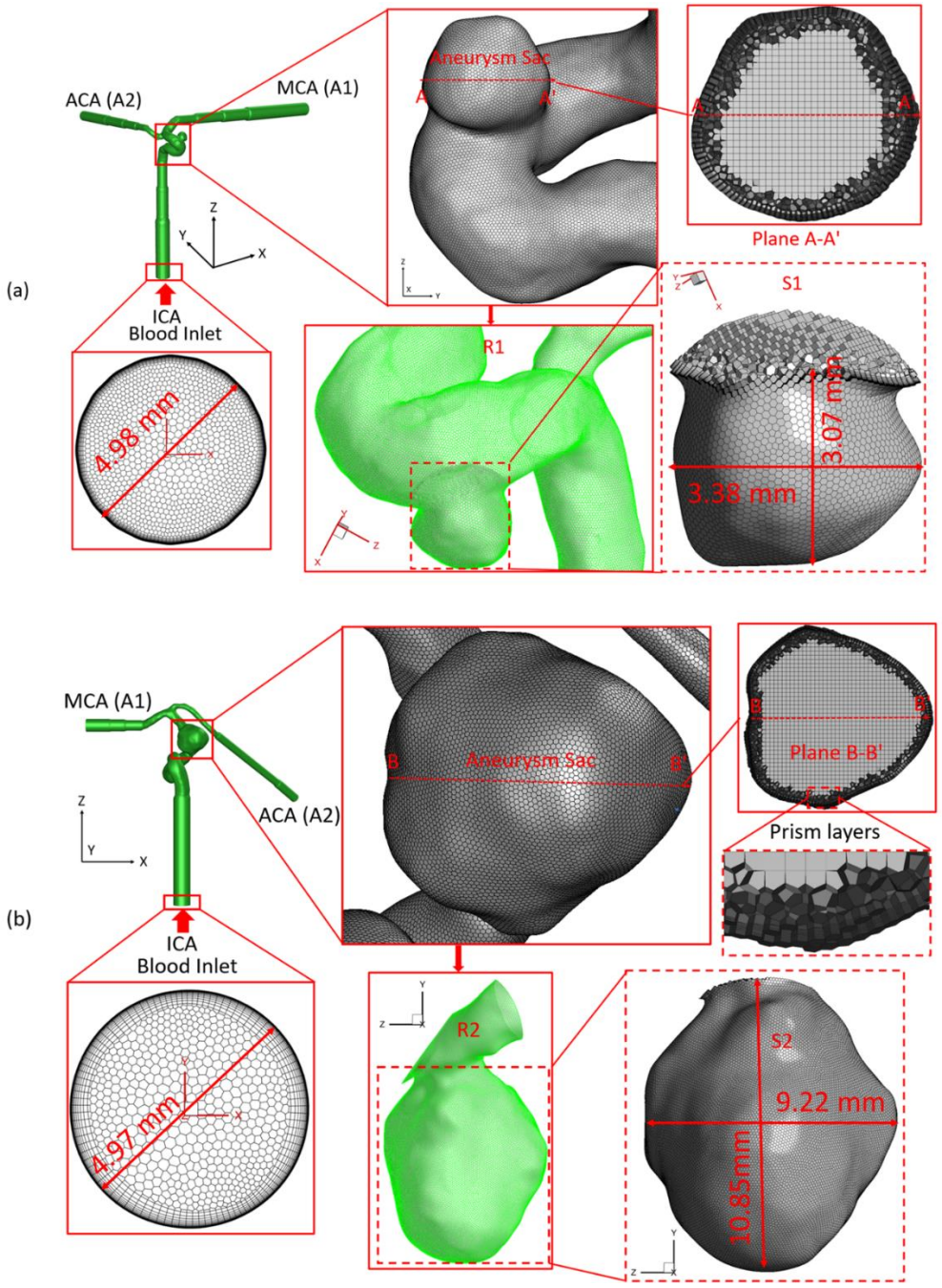

Figure 1. Schematic of the computational domain with hybrid mesh details in ICASA models: (a) ICASA-1, and (b) ICASA-2.

Preprints (www.preprints.org) | NOT PEER-REVIEWED | Posted: 30 May 2022 doi:10.20944/preprints202205.0400.v1

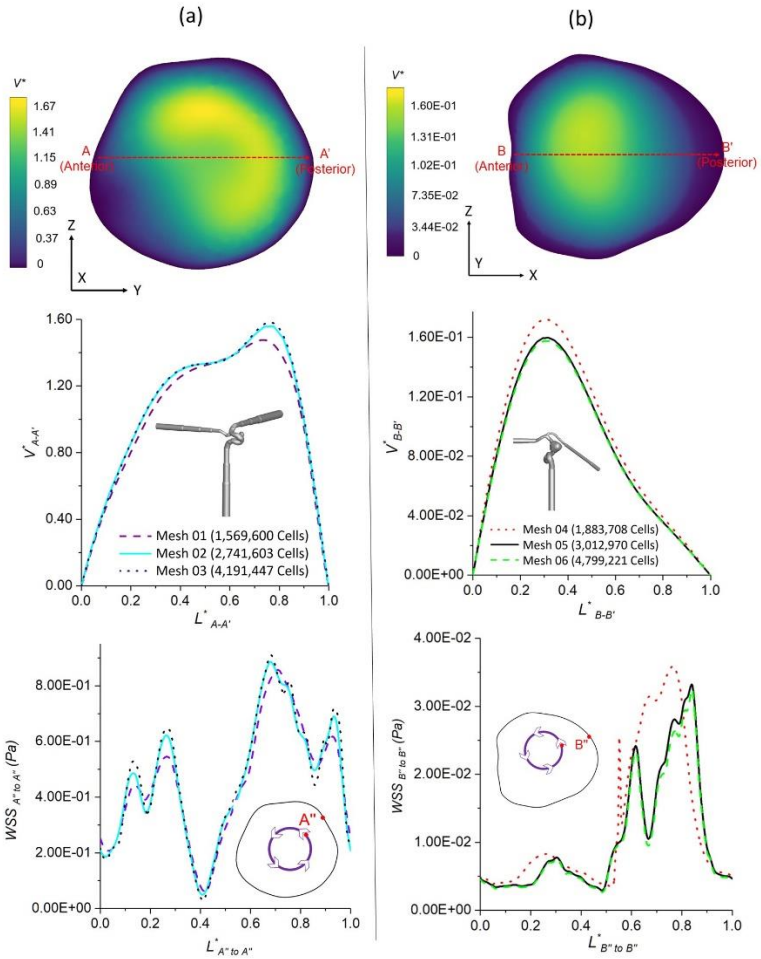

Figure 2. Mesh independence tests for the three cerebral artery aneurysm models: (a) ICASA-1, and (b) ICASA-2.

Table 1. Mesh details in mesh independence tests for the ICASA models.

Mesh	Minimum Size (mm)	Face Elements	Face-Maximum Skewness	Volume Elements	Volume-Maximum Skewness	Prism Layers	Frist Prism Layer Height (m)	Peel Layers	Size Growth Rate
Mesh 01	3.5e-4	31,930	0.45	1,569,600	0.88	15	2.2e-6	3	1.05
Mesh 02 (Final)	3.0e-4	99,170	0.47	2,741,603	0.89	25	1.8e-6		
Mesh 03	2.5e-4	271,511	0.44	4,191,447	0.88	30	1.5e-6		
Mesh 04	4.0e-4	30,589	0.29	1,883,708	0.89	15	2.0e-6		
Mesh 05 (Final)	3.5e-4	126,896	0.42	3,012,970	0.87	20	1.50e-6		
Mesh 06	3.0e-4	166,901	0.38	4,799,221	0.86	25	1.0e-6		

Preprints (www.preprints.org) | NOT PEER-REVIEWED | Posted: 30 May 2022 doi:10.20944/preprints202205.0400.v1

Using different meshes (see **Table 1**), the nondimensionalized velocities and WSS are shown in **Fig. 2**. It can be observed that mesh 01 and mesh 04 are too coarse to generate accurate results. The variations in simulated velocities and WSS are within 1% between mesh 02 and mesh 03. The similar results also can be found with the comparisons in mesh 05 and mesh 06. Thus, based on the optimal balance between computational efficiency and accuracy, mesh 02 (i.e., with 2,741,603 elements, 25 prism layers, 3 peel layers and size growth rate 1.05) and mesh 05 (i.e., with 3,012,970 elements, 20 prism layers, 3 peel layers and size growth rate 1.05) were selected as the final meshes for each ICASA model to study the hemodynamic behaviors.

2.2. Governing Equations

The patient-specific pulsatile blood flow is always unsteady under the action of the periodic pulsatile flow. The continuity and momentum equations can be written in a tensor form, i.e.,

$$\frac{\partial u_i}{\partial x_i} = 0 \tag{4}$$

$$\rho \frac{\partial u_i}{\partial t} + \rho \frac{\partial (u_j u_i)}{\partial x_j} = -\frac{\partial p}{\partial x_i} + \mu \frac{\partial}{\partial x_j}\left[\left(\frac{\partial u_i}{\partial x_j} + \frac{\partial u_j}{\partial x_i}\right)\right] + \rho g_i \tag{5}$$

where u_j represents the blood flow velocity, p is the pressure, g_j is the gravity, μ is blood dynamic viscosity. In this study, the flow regime is assumed as incompressible and Newtonian, the blood density of 1.05e3 kg/m^3 and dynamic viscosity of 3.5e-3 kg/m-s were used. It is worth mentioning that the employed CFD method to simulate blood laminar flow in the cerebral arteries has been well validated with benchmarked experimental data in previous publications [46-52], by the good agreements in comparisons of flow field quantifications.

2.3. Wall Shear Stress (WSS)

Wall shear stress (WSS) plays a significant role in the formation, growth, and rupture of the cerebral aneurysms, which is a tangential frictional force on the arterial wall and induced by the blood shearing. The equation to compute WSS can be written as, i.e.,

$$WSS = \mu \left(\frac{\partial u}{\partial y}\right)_{y=0} \tag{6}$$

where u is the blood velocity parallel to the arterial wall, and y is the normal distance to the arterial wall. To analyze more specifically the WSS effects on the aneurysm sac wall (i.e., S1 in ICASA-1 and S2 in ICASA-2 shown in **Fig. 1**), WSS is divided into three components representing the WSS vector with respect to Cartesian coordinates as follows, e.g.,

$$WSS = WSS_x \vec{i} + WSS_y \vec{j} + WSS_z \vec{k} \tag{7}$$

where WSS_x, WSS_y, WSS_z represents wall stress components in the X, Y, Z direction in Cartesian coordinates. In this study, the surface-average wall shear stress $\overline{WSS}$ in the local aneurysmal region (e.g., R1 in ICASA-1 and R2 in ICASA-2 shown in **Fig. 1**) was also employed to analyze the effects of pulsatile pressures and shunt ratios in bifurcated distal arteries on intra-aneurysmal hemodynamic characteristics, i.e.,

$$\overline{WSS} = \frac{1}{S}\oint |WSS| ds \tag{8}$$

where S is the surface area of selected aneurysmal region.

Preprints (www.preprints.org) | NOT PEER-REVIEWED | Posted: 30 May 2022 doi:10.20944/preprints202205.0400.v1

2.4. Oscillatory Shear Index (OSI)

Oscillatory shear index (OSI) describes the oscillating feature during a pulsatile cycle that is characterized by a nondimensional parameter. It is often employed to describe the disturbance of the flow field in the aneurysm. OSI also shows the magnitude of WSS alterations and illustrates the oscillation of tangential force in one cardiac cycle [53]. The equation to calculate OSI is, i.e.,

$$OSI = \frac{1}{2}\left(1 - \frac{\left|\int_0^T WSSdt\right|}{\int_0^T |WSS|\, dt}\right) \tag{9}$$

where T is the period of one cardiac cycle, i.e., 1.0 s in this study (see **Fig. 3**) The OSI varies between 0 and 0.5 with a value of 0 observed in regions of unidirectional flow and a value of 0.5 observed in regions of fully oscillatory flows.

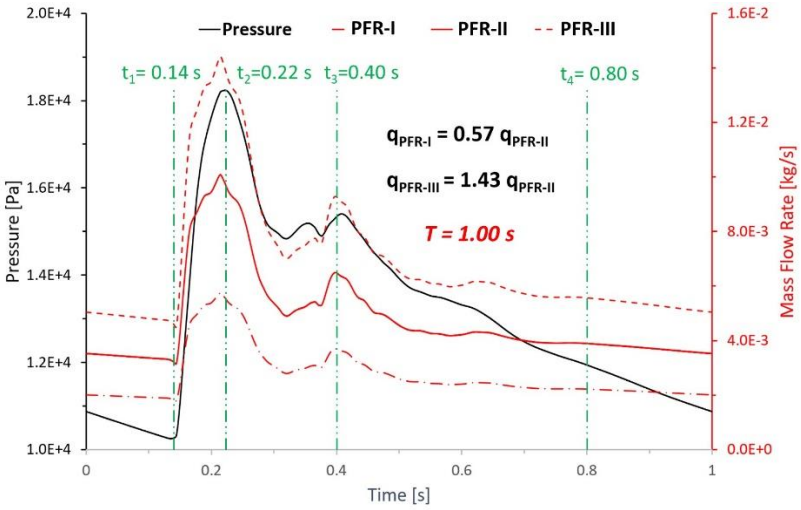

Figure 3. Transient pulsatile flow rate boundary conditions at the internal carotid artery (ICA) inlet.

2.5 Time-averaged Pressure (TAP)

It has been recognized that the high blood pressure can be the major risk factor for the pathophysiology of cerebral aneurysm [54], since the induced hemodynamic stress and inflammation by high blood pressure could lead to arterial wall damage and dilation, then resulting in the growth and rupture of cerebral aneurysms [55, 56]. In this study, the time-averaged pressure (TAP) was calculated under different PFRs and distributions in bifurcated distal arteries, i.e., written as,

$$TAP = \frac{\int_0^T pdt}{T} \tag{10}$$

2.6. Boundary and Initial Conditions

To systematically investigate the PFR effects on the intra-hemodynamic characteristics in the ICASA models, three transient pulsatile flow rate waveforms with a period of T = 1.0 s were applied as the boundary conditions at the ICA inlet (see **Fig. 3**), representing cardiac PFR conditions. Specifically, to study the PFR effects on hemodynamic behaviors in cerebral aneurysms, three different transient pulsatile flow waveforms were employed with different averaged blood flow rates (see **Fig. 3**). As shown in **Fig. 3**, the waveform of PFR-II is based on pulsatile flow rates obtained from 1D model which has been adopted in previous work [44, 57]. According to a statistical study

Preprints (www.preprints.org) | NOT PEER-REVIEWED | Posted: 30 May 2022 doi:10.20944/preprints202205.0400.v1

determining blood flow rates in cerebral arteries [26], another two waveforms, i.e., PFR-I and PFR-III, were generated by multiplying 0.57 and 1.43 times of PFR-II, respectively, which fall into the 95% confidence interval of blood flowrate in ICA based on statistics. It has been found in a previous study that the variation of flow rate in PComA is not significant, and the bifurcated shunt ratio (i.e., flow rate ratio) for ICASA-1 in PComA and ICA distal is approximately close to 25:75 [58]. Thus, this study only investigated the effects of shunt ratios on ICASA-2 model. Specifically, the volumetric shunt ratios (i.e., the minimum and the maximum), q_{A1} *vs.* q_{A2}, e.g., 64:36 [26] and 75:25 [59], were used to investigate the effects of flow-splitting variances in bifurcated distal arteries on hemodynamic behaviors. Additionally, the arterial walls are assumed to be stationary and non-slip, and the blood circulation system is operated under the pressure waveform (see **Fig. 3**) obtained from previous studies [44, 57].

2.7. Numerical Settings

CFD simulations were executed using Ansys Fluent 2021 R2 (Ansys Inc., Canonsburg, PA). All simulation tasks were performed on a local HP Z840 workstation (Intel® Xeon® Processor E5-2687W v4 with dual processors, 24 cores, 48 threads, and 128 GB RAM), and it required ~28 hours to finish the simulation with time step size 5e-4 s for one pulsatile period, i.e., $T = 1.0$ s. Three cardiac periods were simulated for each case and the results were analyzed based on the third period. The Semi-Implicit Method for Pressure Linked Equations (SIMPLE) algorithm was employed for the pressure-velocity coupling, and the least-squares cell-based scheme was applied to calculate the cell gradient. The second order scheme was used for the discretization of pressure and momentum. Convergence is defined for continuity and momentum equations with the residual smaller than 1e-4.

3. RESULTS AND DISCUSSION

3.1. Effects of Pulsatile Flow Rate

To investigate the effects of pulsatile flow rates on hemodynamic characteristics in cerebral aneurysms, the simulation results are compared for three different pulsatile flow rates (e.g., PFR-I, PFR-II, and PFR-III) (see **Fig. 3**) in two patient-specific ICASA models (i.e., ICASA-1 and ICASA-2), respectively. The relationship of three designated pulsatile flow rates is represented by variances of the volumetric flowrates (i.e., $q_{\mathrm{PFR-I}} = 0.57 q_{\mathrm{PFR-II}}$ and $q_{\mathrm{PFR-III}} = 1.47 q_{\mathrm{PFR-II}}$) in the ICA inlet (see **Fig. 3** and **Section 2.6**). Overall, it can be found in the elliptically highlighted regions (red solid lines) of all simulated cases with different pulsatile flow rates and shunt ratios (see **Figs. 4-6**), partial aneurysm neck regions suffers relatively larger WSS than other local regions in both ICASA models, as high as over 300 Pa under the largest pulsatile flow rate (i.e., PFR-III) at the peak systole point (i.e., $t_2 = 0.22$ s) in ICASA-2 model with q_{A1}:q_{A2} = 75:25 (see **Table 2**). This is due to the direct impingements by the blood flow, since part of the blood is redirected into the aneurysm sac from the ICA regime, which was visualized by flow streamlines shown in **Fig. 7**. Also, relatively high OSI distributions can be observed in aneurysmal neck regions where flow separations occur when the blood stream is approaching those regions (see **Fig. 8**). These phenomena indicate that the local neck region in the cerebral aneurysms (highlighted in **Figs. 4-6**) may have higher potential risks to form small or secondary aneurysms, which aligns with the hypothesis that the large WSS integrated with a positive WSS gradient could trigger a mural-cell-mediated pathway that could be allied with the generation, growth and rupture of small or secondary bleb aneurysm phenotypes [16, 60]. On the other hand, the low WSS and high OSI circumstance can be discovered in the highlighted regions with circled dashed lines in **Figs. 4-6** and **8** under all investigated three PFR conditions. These

Preprints (www.preprints.org) | NOT PEER-REVIEWED | Posted: 30 May 2022 doi:10.20944/preprints202205.0400.v1

luminal surfaces could have higher probability to become the enlargement/rupture positions in the aneurysms by inducing inflammatory-cell-mediated destructive remodeling [16].

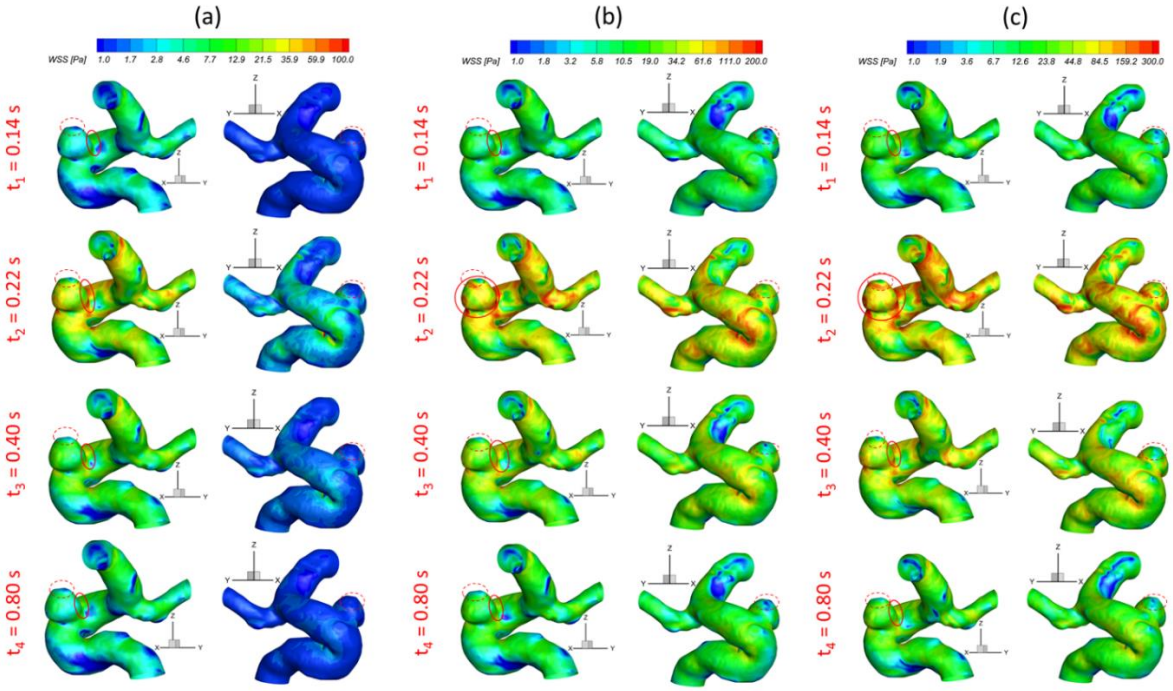

Figure 4. Wall shear stress visualizations on selected region (R1) of ICASA-1 model at selected time instants and bifurcated shunt ratio of q_{A1}:q_{A2} = 75:25 with different pulsatile flow rates: (a) PFR-I, (b) PFR-II, and (c) PFR-III.

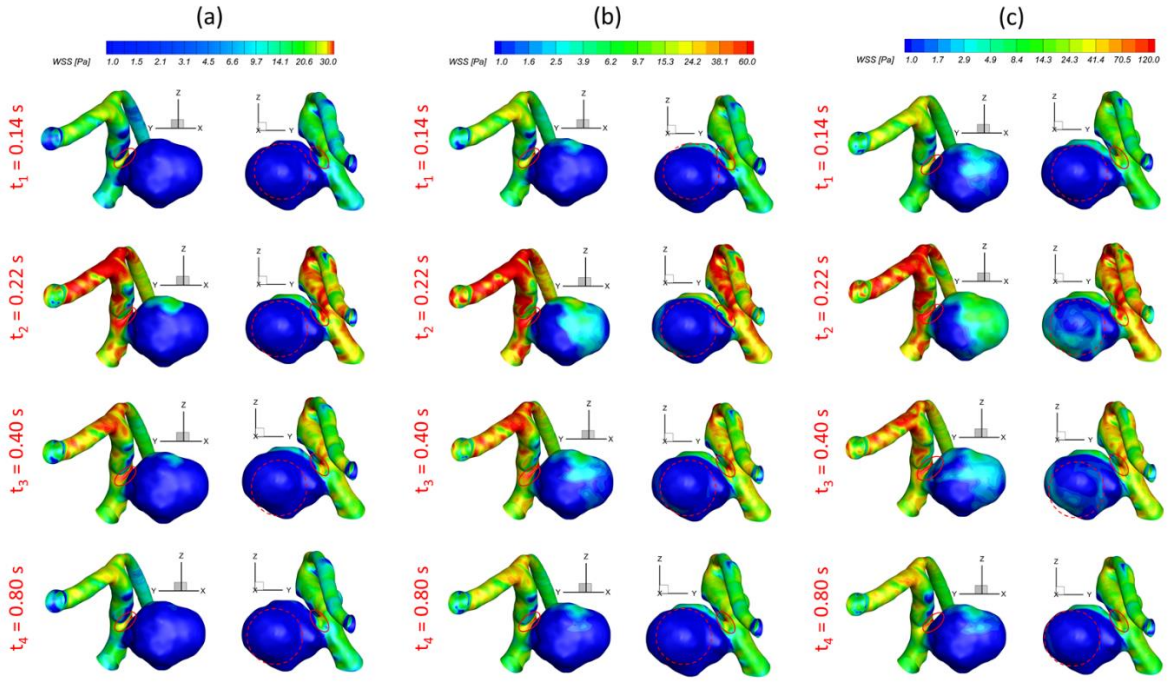

Figure 5. Wall shear stress visualizations on selected region (R2) of ICASA-2 model at selected time instants and bifurcated shunt ratio of q_{A1}:q_{A2} = 75:25 with different pulsatile flow rates: (a) PFR-I, (b) PFR-II, and (c) PFR-III.

Preprints (www.preprints.org) | NOT PEER-REVIEWED | Posted: 30 May 2022 doi:10.20944/preprints202205.0400.v1

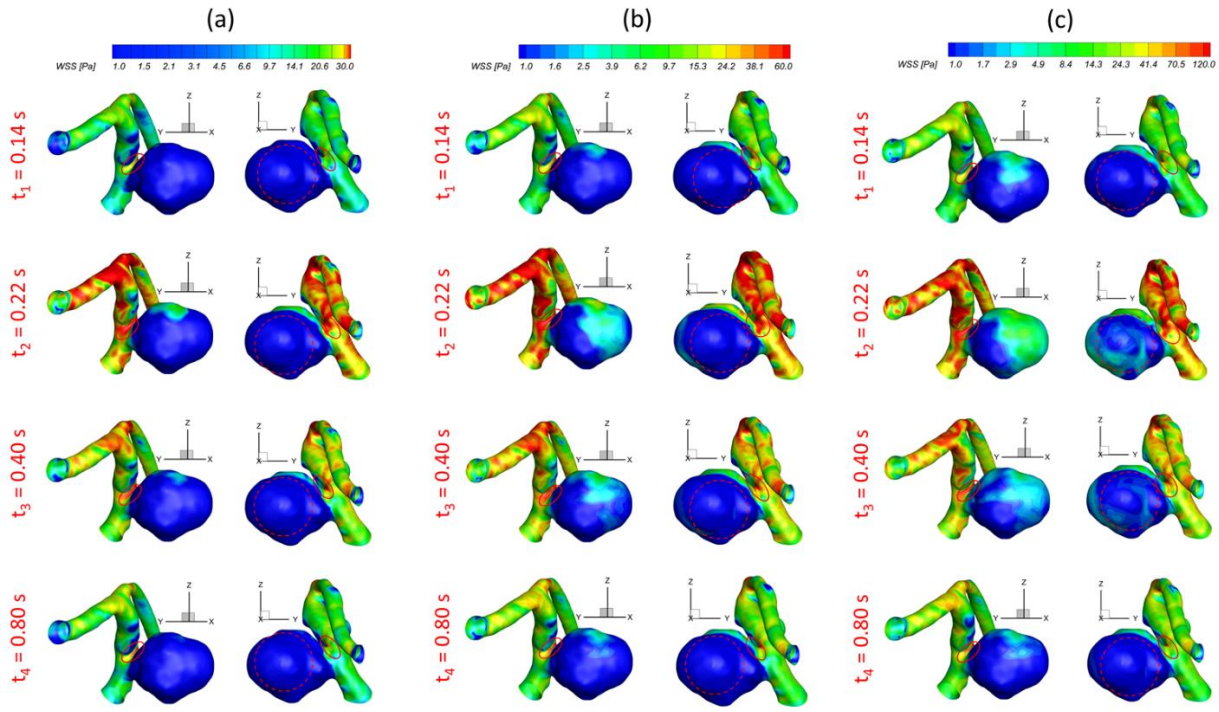

Figure 6. Wall shear stress visualizations on selected region (R2) of ICASA-2 model at selected time instants and bifurcated shunt ratio of q_{A1}:q_{A2} = 64:36 with different pulsatile flow rates: (a) PFR-I, (b) PFR-II, and (c) PFR-III.

Figures 4 (a), (b) & (c) manifest noticeable differences among the pulsatile flow rates in calculations of WSS in the aneurysmof ICASA-1 model under selected time instants, and the similar phenomena can be found in ICASA-2 model (see **Figs. 5 & 6**). The CFD simulation results (see **Figs. 4-6**) show that the larger pulsatile flow rate (i.e., PFR-III) leads to larger WSS than smaller pulsatile flow rates (i.e., PFR-I and PFR-II) in all simulated cases at the same bifurcated shunt ratio. **Tables 2** and **3** show the same phenomena with more detailed WSS calculations (i.e., maximum WSS and minimum WSS in corresponded axis directions in S1 and S2, and surface averaged $\overline{WSS}$ in R1 and R2) at representative time instants. Such an increase in WSS for the patients with a large pulsatile flow rate could facilitate the higher probability of secondary aneurysm generation and/or thin-wall symptoms in the existing aneurysm, since the ICA wall tension/deformation may increase and then overcome the wall tissue compliance, which is consistent with the perspectives from previous studies [61, 62]. Quantitatively, at time instants t_1 = 0.12 s, t_1 = 0.22 s, t_3 = 0.40 s, and t_4 = 0.80 s, the surface-averaged wall shear stresses $\overline{WSS}$ under PFR-II and PFR-III are about one and three times larger than the $\overline{WSS}$ under PFR-I at the region near the aneurysmal sac (R1) of ICASA-1 model, respectively (see **Table 3**). The similar ratios can also be observed at the same time instants in R2 of ICASA-2 model shown in **Table 3**. These comparable discoveries can be explained well with the classic fluid dynamic theory [63] that the larger flow rate can lead to a larger velocity gradient (see **Eq. (6)**) within the boundary layer near the arterial wall surface. The increased near-surface velocity gradient in these regions gives rise to larger viscous shear stresses on the aneurysmal wall. These phenomena can be further explained directly based on the comparisons in velocity profiles in the ICASA models. At t_2 = 0.22 s, the nondimensionalized velocity magnitude V^* at the selected lines (i.e., lines a, b,

Preprints (www.preprints.org) | NOT PEER-REVIEWED | Posted: 30 May 2022 doi:10.20944/preprints202205.0400.v1

Table 2. Maximum wall shear stress WSS in the aneurysm sacs (S1 and S2) under the bifurcated shunt ratio q_{A1}:q_{A2} = 75:25 and different pulsatile flow rates at designated time instants.

Aneurysmal Sac	PFR	WSS Categories	Time Instant (s)			
			t_1 = 0.14	t_2 = 0.22	t_3 = 0.40	t_4 = 0.80
ICASA-1 (S1)	PFR-I	WSS_{Max}	15.2711	173.537	40.8334	19.869
		WSS_{x_Max}	-9.98615	-81.9959	-34.0993	-13.9671
		WSS_{y_Max}	13.3374	73.5389	36.5139	17.596
		WSS_{z_Max}	12.1799	91.7417	32.5699	16.5839
	PFR-II	WSS_{Max}	43.3625	267.123	122.726	59.102
		WSS_{x_Max}	-29.8159	-220.707	-96.8994	-41.3871
		WSS_{y_Max}	32.3394	191.372	90.6823	42.4013
		WSS_{z_Max}	36.2225	231.593	108.234	50.3479
	PFR-III	WSS_{Max}	80.9053	431.082	231.061	108.233
		WSS_{x_Max}	-58.853	-361.069	-194.217	-82.4116
		WSS_{y_Max}	56.5928	249.25	154.078	74.6838
		WSS_{z_Max}	71.5142	391.926	206.949	98.4345
ICASA-2 (S2)	PFR-I	WSS_{Max}	34.0782	169.003	92.7069	45.3113
		WSS_{x_Max}	-22.7832	-87.9672	-54.4009	-28.8848
		WSS_{y_Max}	25.3666	116.035	68.6824	32.9661
		WSS_{z_Max}	24.1866	135.185	69.7968	32.8628
	PFR-II	WSS_{Max}	86.1642	343.389	213.202	107.149
		WSS_{x_Max}	-52.2246	-146.942	-107.226	-60.6988
		WSS_{y_Max}	60.534	234.625	153.317	75.4735
		WSS_{z_Max}	63.318	269.778	174.383	84.017
	PFR-III	WSS_{Max}	138.585	587.266	321.377	175.407
		WSS_{x_Max}	-77.2774	-276.796	-130.745	-82.6379
		WSS_{y_Max}	98.1775	392.104	214.711	117.631
		WSS_{z_Max}	109.770	438.358	251.712	140.801

and c in ICASA-1, and lines d and e in ICASA-2) are shown in **Figs. 9 (a) & (b)**, respectively. As shown by the comparisons made among the three velocity profiles near the artery wall that are enlarged and shown in **Fig. 9**, the higher pulsatile flow rate results in a steeper slope (i.e., larger velocity gradient), and then leads to larger WSS on the selected aneurysmal wall, along with stronger wall impingements by the bulkier blood flows (see **Fig. 7**). The circled regions in the velocity vector distributions in **Fig. 10** also support this explanation. Conversely, a smaller blood flow rate causes less blood stream entering the aneurysmal sac (see **Figs. 10 (a), (d) and (g))** and thus smaller velocity

Preprints (www.preprints.org) | NOT PEER-REVIEWED | Posted: 30 May 2022 doi:10.20944/preprints202205.0400.v1

gradients on the arterial wall (see **Figs. 9 (a) & (b)**). Also, such explanation reveals that the differences in comparisons of $\overline{WSS}$ at t_1 = 0.12 s among PFR-I, PFR-II, and PFR-III are much smaller than other designated time instants, e.g., t_2, t_3, and t_4 (see **Fig. 3**).

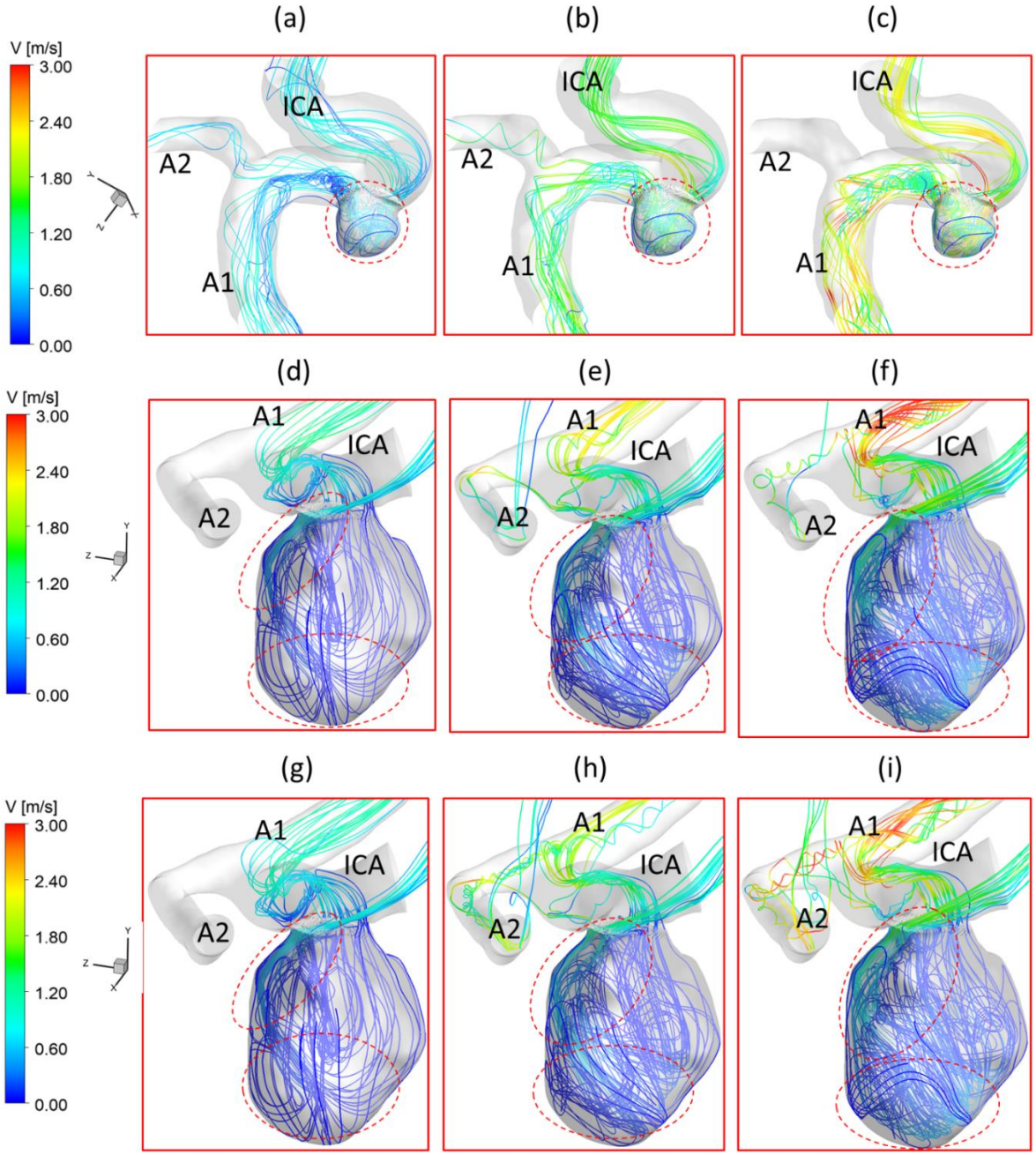

Figure 7. Visualized flow streamlines in ICASA-1 (S1) and ICASA-2 (S2) models under different conditions at t_2 = 0.13 s: (a) ICASA-1, q_{A1}:q_{A2} = 75:25, and PFR-I, (b) ICASA-1, q_{A1}:q_{A2} = 75:25, and PFR-II, (c) ICASA-1, q_{A1}:q_{A2} = 75:25, and PFR-III, (d) ICASA-2, q_{A1}:q_{A2} = 75:25, and PFR-I, (e) ICASA-2, q_{A1}:q_{A2} = 75:25, and PFR-II, (f) ICASA-2, q_{A1}:q_{A2} = 75:25, and PFR-III, (g) ICASA-2, q_{A1}:q_{A2} = 64:36, and PFR-I, (h) ICASA-2, q_{A1}:q_{A2} = 64:36, and PFR-II, and (i) ICASA-2, q_{A1}:q_{A2} = 64:36, and PFR-III.

Preprints (www.preprints.org) | NOT PEER-REVIEWED | Posted: 30 May 2022 doi:10.20944/preprints202205.0400.v1

Table 3. Surface-averaged wall shear stress $\overline{WSS}$ (Pa) in aneurysmal regions (R1 and R2) under selected time instants and boundary conditions.

Selected Region	q_{A1}:q_{A2}	Pulsatile Flow Rate	Time Instant (s)			
			t_1 = 0.14	t_2 = 0.22	t_3 = 0.40	t_4 = 0.80
			$\overline{WSS}$ (Pa)			
ICASA-1 (R1)	75:25	PFR-I	3.783	19.230	9.586	4.933
		PFR-II	8.752	46.121	22.782	11.310
		PFR-III	15.105	82.072	39.916	19.736
ICASA-2 (R2)	75:25	PFR-I	2.359	11.390	6.264	3.061
		PFR-II	5.292	26.509	13.909	6.900
		PFR-III	8.989	44.884	23.743	11.518
	64:36	PFR-I	2.543	11.863	6.402	3.282
		PFR-II	5.594	27.110	14.258	7.180
		PFR-III	9.306	46.224	23.961	11.729

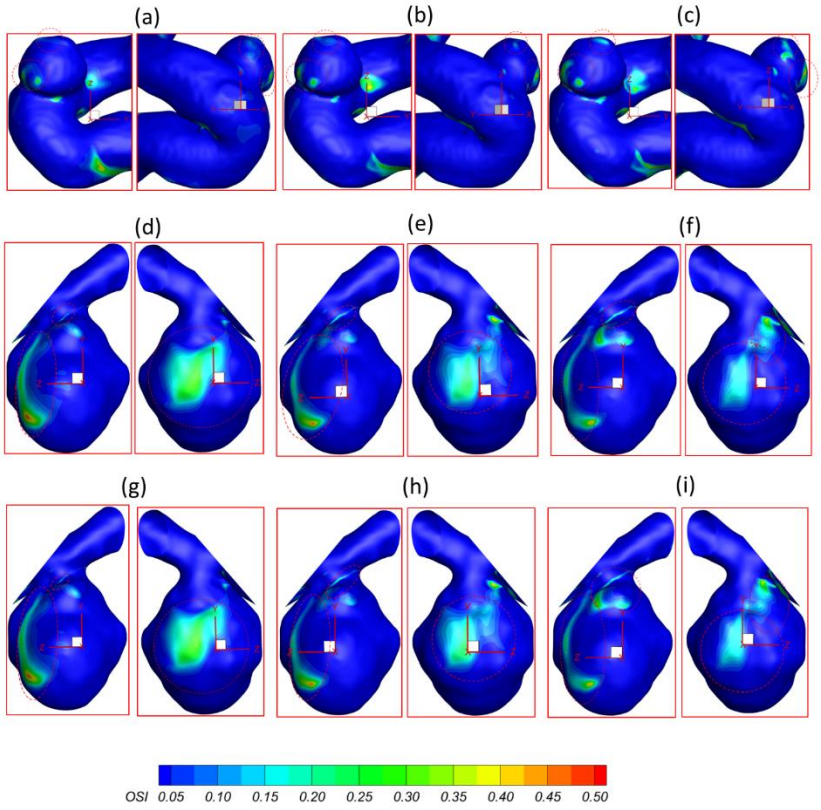

Figure 8. OSI distributions in ICASA-1 and ICASA-2 models under different conditions: (a) ICASA-1, q_{A1}:q_{A2} = 75:25, and PFR-I, (b) ICASA-1, q_{A1}:q_{A2} = 75:25, and PFR-II, (c) ICASA-1, q_{A1}:q_{A2} = 75:25, and PFR-III, (d) ICASA-2, q_{A1}:q_{A2} = 75:25, and PFR-I, (e) ICASA-2, q_{A1}:q_{A2} = 75:25, and PFR-II, (f) ICASA-2, q_{A1}:q_{A2} = 75:25, and PFR-III, (g) ICASA-2, q_{A1}:q_{A2} = 64:36, and PFR-I, (h) ICASA-2, q_{A1}:q_{A2} = 64:36, and PFR-II, and (i) ICASA-2, q_{A1}:q_{A2} = 64:36, and PFR-III.

Preprints (www.preprints.org) | NOT PEER-REVIEWED | Posted: 30 May 2022 doi:10.20944/preprints202205.0400.v1

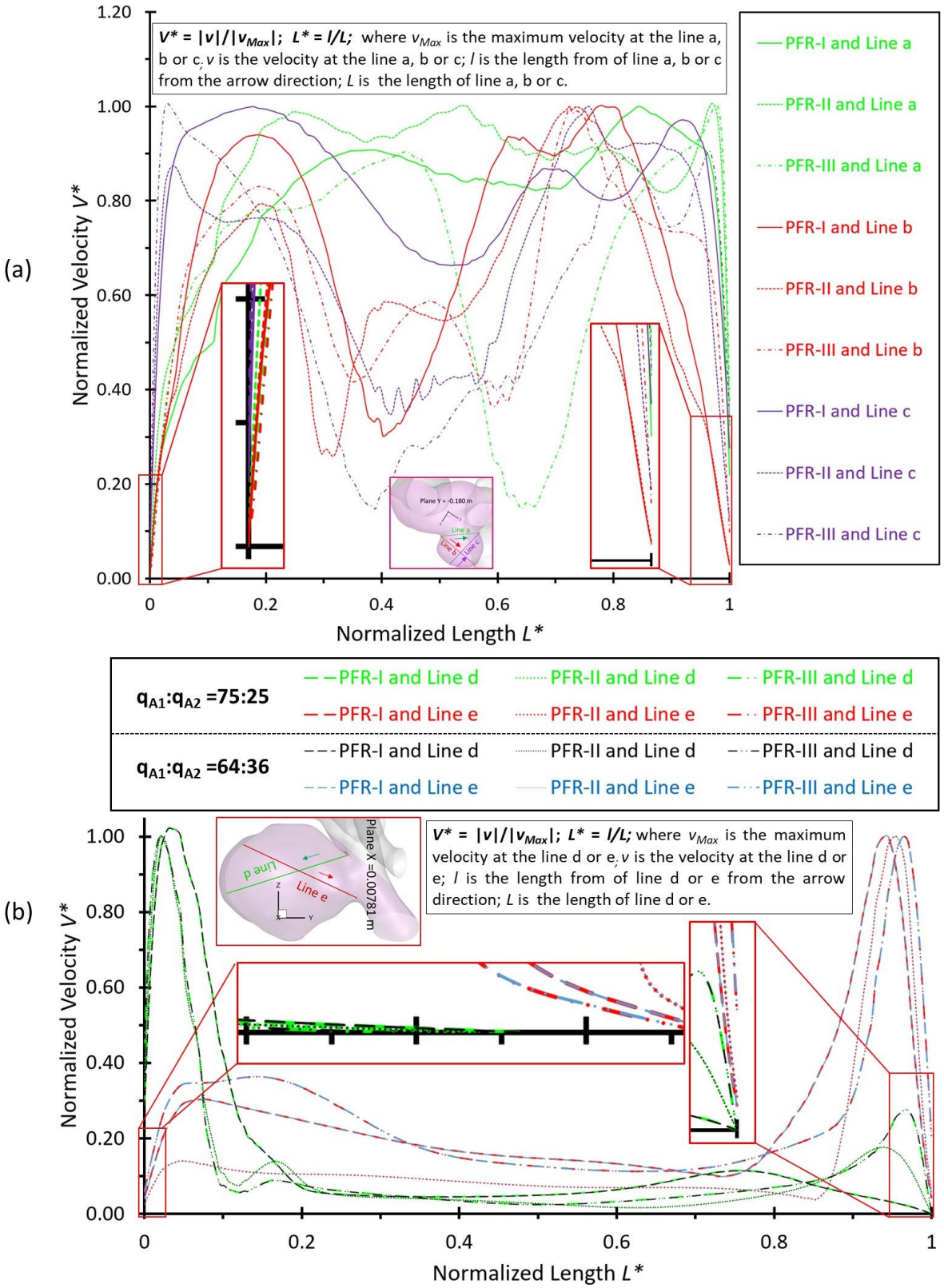

Figure 9. Nondimensionalized velocity profiles V^* at the designated cross lines across the aneurysmal sac at t_2 = 0.22 s in ICASA models: (a) ICASA-1, and (b) ICASA-2.

Preprints (www.preprints.org) | NOT PEER-REVIEWED | Posted: 30 May 2022 doi:10.20944/preprints202205.0400.v1

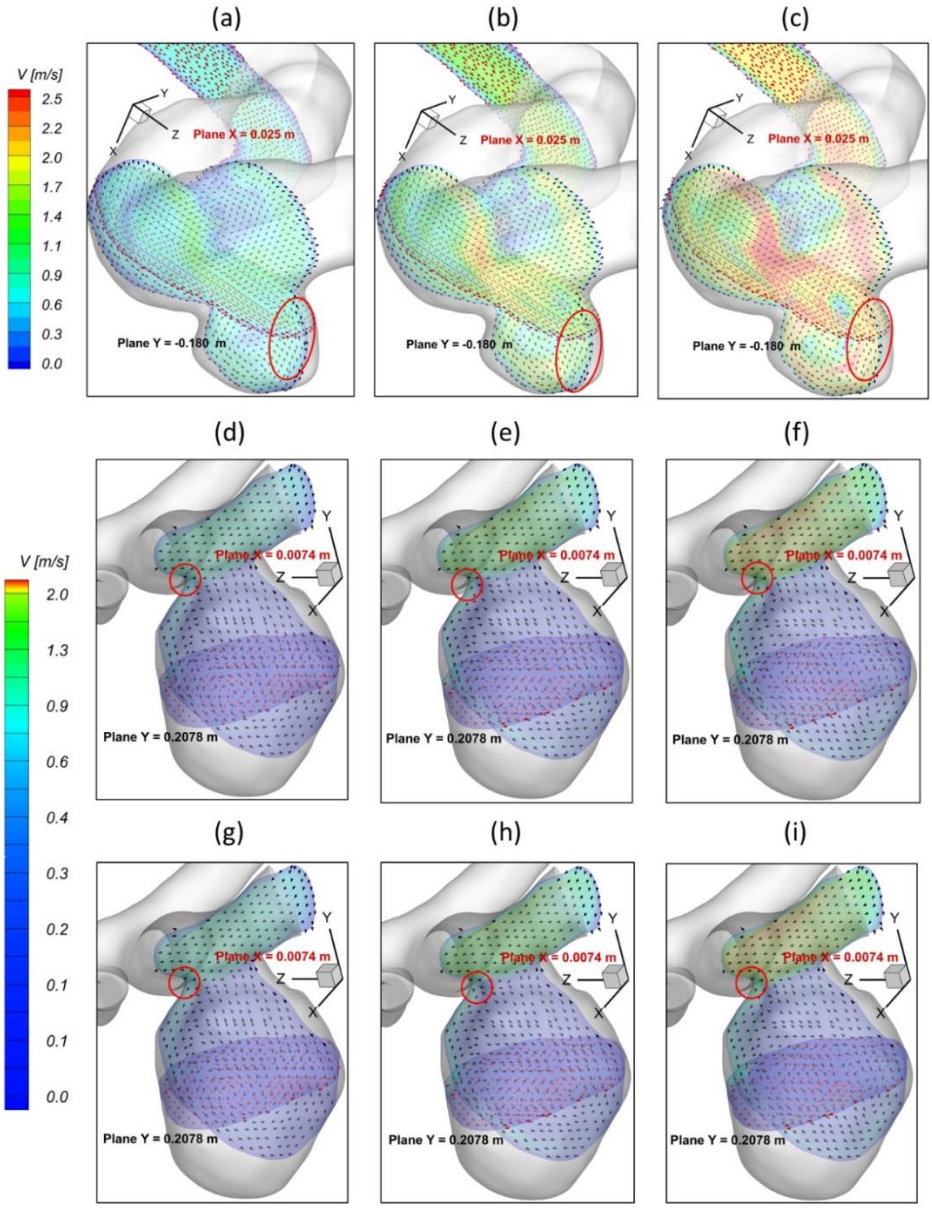

Figure 10. Visualized velocity profiles at t_2 = 0.22 s in selected planes of ICASA models: (a) ICASA-1, q_{A1}:q_{A2} = 75:25, and PFR-I, (b) ICASA-1, q_{A1}:q_{A2} = 75:25, and PFR-II, (c) ICASA-1, q_{A1}:q_{A2} = 75:25, and PFR-III, (d) ICASA-2, q_{A1}:q_{A2} = 75:25, and PFR-I, (e) ICASA-2, q_{A1}:q_{A2} = 75:25, and PFR-II, (f) ICASA-2, q_{A1}:q_{A2} = 75:25, and PFR-III, (g) ICASA-2, q_{A1}:q_{A2} = 64:36, and PFR-I, (h) ICASA-2, q_{A1}:q_{A2} = 64:36, and PFR-II, and (i) ICASA-2, q_{A1}:q_{A2} = 64:36, and PFR-III.

It should not be neglected that although the smaller pulsatile flow rate may influence the aneurysm sac insignificantly when considering the low *WSS* solely (see **Figs. 4 (a), 5 (a), & 6 (a)**), the *OSI* is still high on a larger surface area at some local regions, i.e., especially on the fundus of the aneurysm dome (see **Figs. 8 (a), (d), & (g)**), under such small pulsatile flow rate (i.e., PFR-I) than its counterparts under large pulsatile flow rate (e.g., PFR-II and PFR-III) (see **Figs. 8 (b), (c), (e), (f), (h), & (i)**). Low *WSS* and high *OSI* are well known as a leading hypothesis to trigger growth

Preprints (www.preprints.org) | NOT PEER-REVIEWED | Posted: 30 May 2022 doi:10.20944/preprints202205.0400.v1

and rupture of cerebral aneurysms *via.* malfunctioning endothelial surface to produce nitric oxide, increasing endothelial permeability, and consequently promoting inflammatory cell infiltration [64-67]. Thus, reducing OSI in some local regions (highlighted in **Fig. 8**) for patients with a smaller pulsatile flow rate should be an important concern when the clinicians consider treatments to decrease the risks of aneurysmal sac rupture. For instance, the stents and coils should be placed in appropriate locations and directions that can alter flow patterns and then reduce OSI on these special regions of an aneurysmal dome.

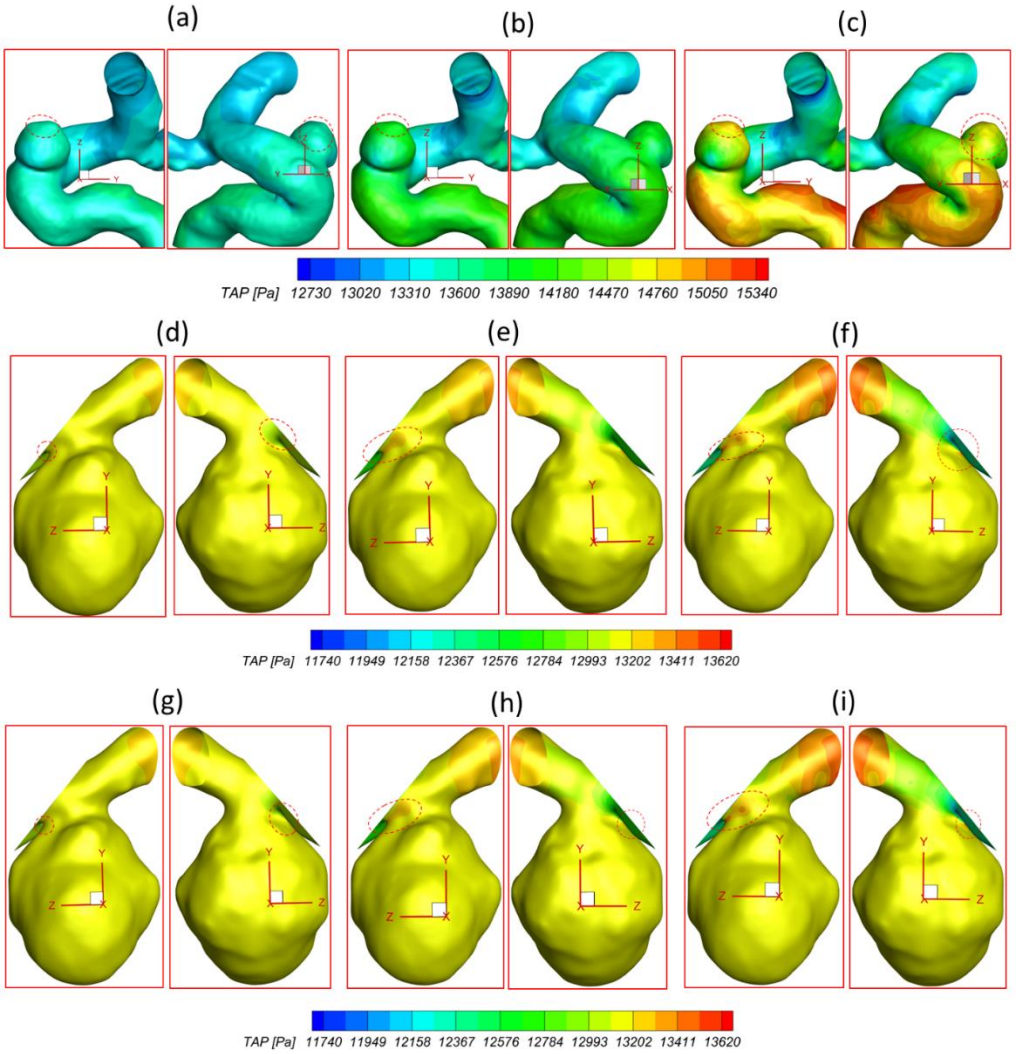

Figure 11. TAP distributions on the wall of ICASA models: (a) ICASA-1, q_{A1}:q_{A2} = 75:25, and PFR-I, (b) ICASA-1, q_{A1}:q_{A2} = 75:25, and PFR-II, (c) ICASA-1, q_{A1}:q_{A2} = 75:25, and PFR-III, (d) ICASA-2, q_{A1}:q_{A2} = 75:25, and PFR-I, (e) ICASA-2, q_{A1}:q_{A2} = 75:25, and PFR-II, (f) ICASA-2, q_{A1}:q_{A2} = 75:25, and PFR-III, (g) ICASA-2, q_{A1}:q_{A2} = 64:36, and PFR-I, (h) ICASA-2, q_{A1}:q_{A2} = 64:36, and PFR-II, and (i) ICASA-2, q_{A1}:q_{A2} = 64:36, and PFR-III.

With respect to the PFR effects on the blood pressure, the highlighted regions **in Figures 11 (a)-(c)** and **Table 4** manifest that larger PFR (i.e., PFR-III) leads to relatively higher TAP on the aneurysmal wall since more blood is redirected into the aneurysm sac from the ICA regime, which causes higher velocity impingement on the sac wall (see

Preprints (www.preprints.org) | NOT PEER-REVIEWED | Posted: 30 May 2022 doi:10.20944/preprints202205.0400.v1

Figs. 7 (a)-(c) and **Figs. 10 (a)-(c)**), and then leads to higher blood pressure than the other two smaller PFRs at the same time instants. The high blood pressure associated with the larger PFR can be a potential risk factor for the pathophysiology of cerebral aneurysm [54], since the induced hemodynamic stress and inflammation by high blood pressure could result in the growth and rupture of cerebral aneurysm by causing arterial wall damage and dilation [55, 56]. Nevertheless, it still can be interestingly found in **Figs. 11 (a)-(i)** that the variance of PFR has no extremely significant impact on TAP distributions on the aneurysmal dome wall in both ICASA models, since comparing to the static pressure, the contribution from dynamic pressure is insignificant to affect the total blood pressure intrinsically. Specifically, TAP distributions vary from 13310 to 15050 Pa on the aneurysmal wall in ICASA-1 and 13097 to 13202 Pa on the aneurysmal wall in ICASA-2, respectively. Some local regions close to the lower portions of the aneurysmal neck (highlighted with dash lines) in ICASA-2 register relatively higher TAP (i.e., 13202 to 13411 Pa) which is because the local velocity at these regions is higher than other regions in the sac, where TAP is distributed relatively uniform (i.e., nearly 13000 Pa) due to smaller velocity differences under the three PFRs (see **Figs. 7 (d)-(i)** and **Figs. 10 (d)-(i)**).

Table 4. Time averaged pressure TAP (Pa) in aneurysmal regions (R1 and R2) at different flow rates.

Selected Region	q_{A1}:q_{A2}	Pulsatile Flow Rate	TAP (Pa)	
			Minimum	Maximum
ICASA-1 (R1)	75:25	PFR-I	13114.6	13613.0
		PFR-II	12973.9	14301.0
		PFR-III	12732.1	153.24.9
ICASA-2(R2)	75:25	PFR-I	12884.3	13262.5
		PFR-II	12399.9	13429.7
		PFR-III	11742.8	13613.9
	64:36	PFR-I	12884.4	13263.0
		PFR-II	12400.0	13430.0
		PFR-III	11743.3	13614.2

3.2. Effects of Shunt Ratios in Bifurcated Distal Arteries

To analyze hemodynamic characteristics in aneurysms due to different shunt ratios in the bifurcated A1 and A2, CFD results are compared using two shunt ratios of q_{A1}:q_{A2}, e.g., 75:25 and 64:36, in the patient-specific ICASA-2 model. Specifically, the simulation results of WSS (see **Figs. 5 & 7**), velocity streamlines (see **Figs. 7 (d)-(i)**), OSI (see **Figs. 8 (d)-(i)**), nondimensionalized velocity profiles on selected lines (see **Fig. 9 (b)**), velocity vectors in selected slices (see **Figs. 10 (d)-(i))**, and TAP distributions (see **Figs. 11 (d)-(i)**) are compared between the two shunt ratios (i.e., 75:25 and 64:36), respectively. Overall, it can be observed that the flow rates in A1 and A2 nearly have minimal effects on blood flow field in the aneurysmal sac. All above-mentioned comparable parameters (i.e., WSS, TAP, velocity profiles, and OSI) at the two ratios showed nearly identical distributions in cerebral aneurysm sac under the same pulsatile flow rate. Such limited influence on flow patterns in the aneurysmal dome by the variance of shunt ratios in bifurcated distal arteries is because of the fact that the distance from the aneurysmal sac to the bifurcation

Preprints (www.preprints.org) | NOT PEER-REVIEWED | Posted: 30 May 2022 doi:10.20944/preprints202205.0400.v1

point is too far to alternate the blood flow patterns in the dome. The only minor difference of the averaged wall shear stress $\overline{WSS}$ and TAP is observed in the studied aneurysmal region, R2. $\overline{WSS}$ under q_{A1}:q_{A2} = 75:25 is a little bit smaller than the counterparts under q_{A1}:q_{A2} = 64:36 at designated time instants (**see Table V**), which is due to the fact that the integral scope to compute $\overline{WSS}$ not only contains the aneurysmal sac, but also takes partial arterial walls of ICA, A1 and A2 into consideration (see **Figs. 10 & 11)**. This fact also can explain the minor differences in TAP under the two ratios (see **Table 4**).

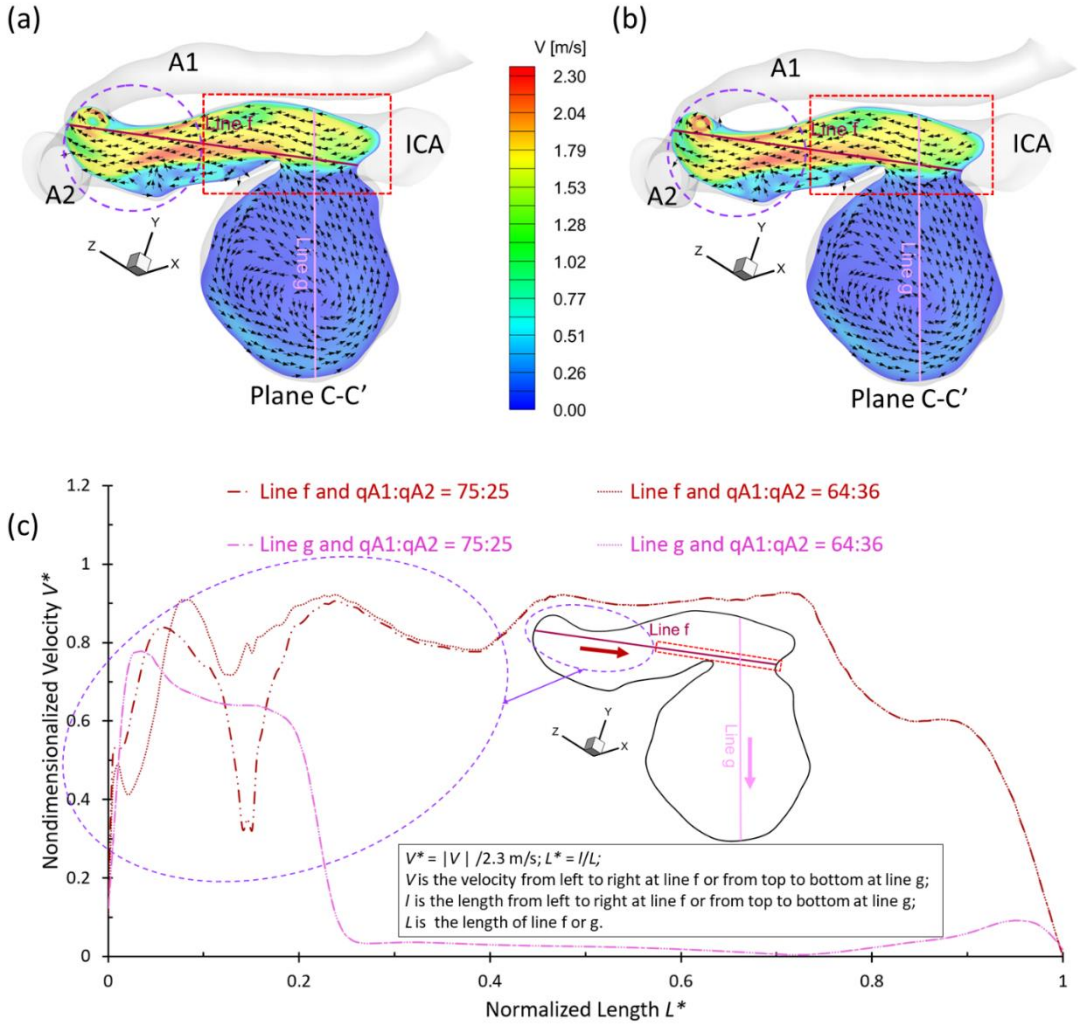

Figure 12. Comparisons of velocity profiles in selected plane C-C' and velocity distributions in selected lines f and g in ICASA-2 model under different bifurcated shunt ratios: (a) velocity profiles at plane C-C' under q_{A1}:q_{A2} = 75:25, and (b) velocity profiles at plane C-C' under q_{A1}:q_{A2} = 64:36, and nondimensionalized velocity profiles at lines g and f.

To investigate more specifically the critical distance from the bifurcated arteries (i.e., A1 and A2) to the aneurysmal sac beyond which the variance of shunt ratio can influence the flow patterns in the brain aneurysm model (i.e., ICASA-2), the flow details in this region have been visualized in the designated plane C-C' in **Fig. 12** at the time instant of t_2

Preprints (www.preprints.org) | NOT PEER-REVIEWED | Posted: 30 May 2022 doi:10.20944/preprints202205.0400.v1

= 0.22 s under PFR-II. **Figs. 12 (a) & (b)** show velocity magnitude contours under the two-shunt ratios, i.e., q_{A1}:q_{A2} = 75:25 and q_{A1}:q_{A2} = 64:36, respectively. It can be found that the red colored rectangular region has the same flow field under both shunt ratios, in accordance with the nondimensionalized velocity profiles along the selected line f (see **Fig. 12 (c)**). The visualized velocity profiles along the designated line g (colored with pink) also support the observation that V^* profiles are identical under the two distributed ratios shown in **Fig. 12 (c)**. The flow patterns begin to differ in the two ratios when L^* is smaller than 0.405 (see **Fig. 12 (c)**). It implies that only the aneurysmal sac is formed close enough to the bifurcated arteries, i.e., $0 < L^* \leq 0.405$ in ICASA-2 model, the difference of shunt ratios in bifurcated distal arteries can show a noticeable impact on the blood transport behaviors in the aneurysm. The discoveries in this study may help the clinicians obtain more accurate information when the treatments are attempted for patients with cerebral aneurysm issues which are closely approaching the bifurcated arteries. Nevertheless, it should be mentioned that the critical value L^* may vary with the PFR conditions, and the qualitatively and quantitatively statistic investigations on effects of bifurcated blood distributions on WSS and OSI in the aneurysm still need to be conducted based on the patient-specific cerebral aneurysms (e.g., close enough to the bifurcated arteries) in future studies.

3.3. Effects of Transitional Pulsatile Blood Flow

During a single cardiac pulse period, i.e., T = 1.0 s, the WSS on arterial walls and blood flow patterns in the aneurysmal sac vary with the flow rate. As shown in **Fig. 3**, the blood flow rate drops slowly form the beginning to 0.14 s, then increases sharply to the maximum at t_2 = 0.22 s and follows with a steep decrease and experiences an oscillation to the second largest peak during 0.22 s to 0.44 s, and declines gradually till one cardiac period is concluded. Meanwhile, in one cardiac period, the induced WSS in the aneurysm sac presents a similar trend as the transient pulsatile flow rate waveform, showing that the larger volumetric flow rate induces larger velocity gradient, thus leads to larger WSS on the aneurysmal sac wall. Specifically, the maximum WSS appears at t_2 = 0.22 s with 587.266 Pa under PFR-III with q_{A1}:q_{A2} = 75:25 (see **Figs. 6**, and **Table 2**) in ICASA-2 model, while the minimum WSS is 15.27 Pa under PFR-1 with qA1:qA2 = 75:25 in ICASA-1 model. However, comparing the surface-averaged $\overline{WSS}$, the maximum value of 82.072 Pa appears at the designated region (e.g., R1 in ICASA-1) at the peak systole i.e., t_2 = 0.22 s) (see **Table 3**). This is because of the selected integral region for calculation of the $\overline{WSS}$ and it has been explained in **Section 3.2**. More specifically, for an instance, during one cardiac period in the two investigated ICASA models under PFR-II and q_{A1}:q_{A2} = 75:25 (see **Table 2**), the maximum WSS are 43.36, 267.12, 122.73, and 59.10 Pa on the sac of ICASA-1 (S1) and 86.16, 343.39, 213.20, and 107.15 Pa on the sac of the ICASA-2 (S2) under the three mass flow rates at the representative time instants (i.e., t_1 = 0.14 s, t_2 = 0.22 s, t_3 = 0.40 s, and t_4 = 0.80 s) are 3.18e-3, 9.93e-3, 6.48e-3, and 3.89e-3 kg/s, respectively. As the mass flow rate increases about two times from the flowing time t_1 to t_2, while its corresponding maximum WSS and $\overline{WSS}$ increase over four times in ICASA-1 and three times in ICASA-2 in all studied PFRs, respectively. Such results are due to the fact that the velocity gradient increases more intensively as the blood flow rate increase during one pulse period. These findings may provide guidelines to consult some patients with CAs to avoid aggressive sports and exercises since the blood flow rate during maximum exercise may increase to 4 times of the value for the rest state [68]. The significantly increased flow rate can cause much higher WSS on the aneurysmal wall and then pose potential risks to facilitate the aneurysm growth or rupture.

Preprints (www.preprints.org) | NOT PEER-REVIEWED | Posted: 30 May 2022 doi:10.20944/preprints202205.0400.v1

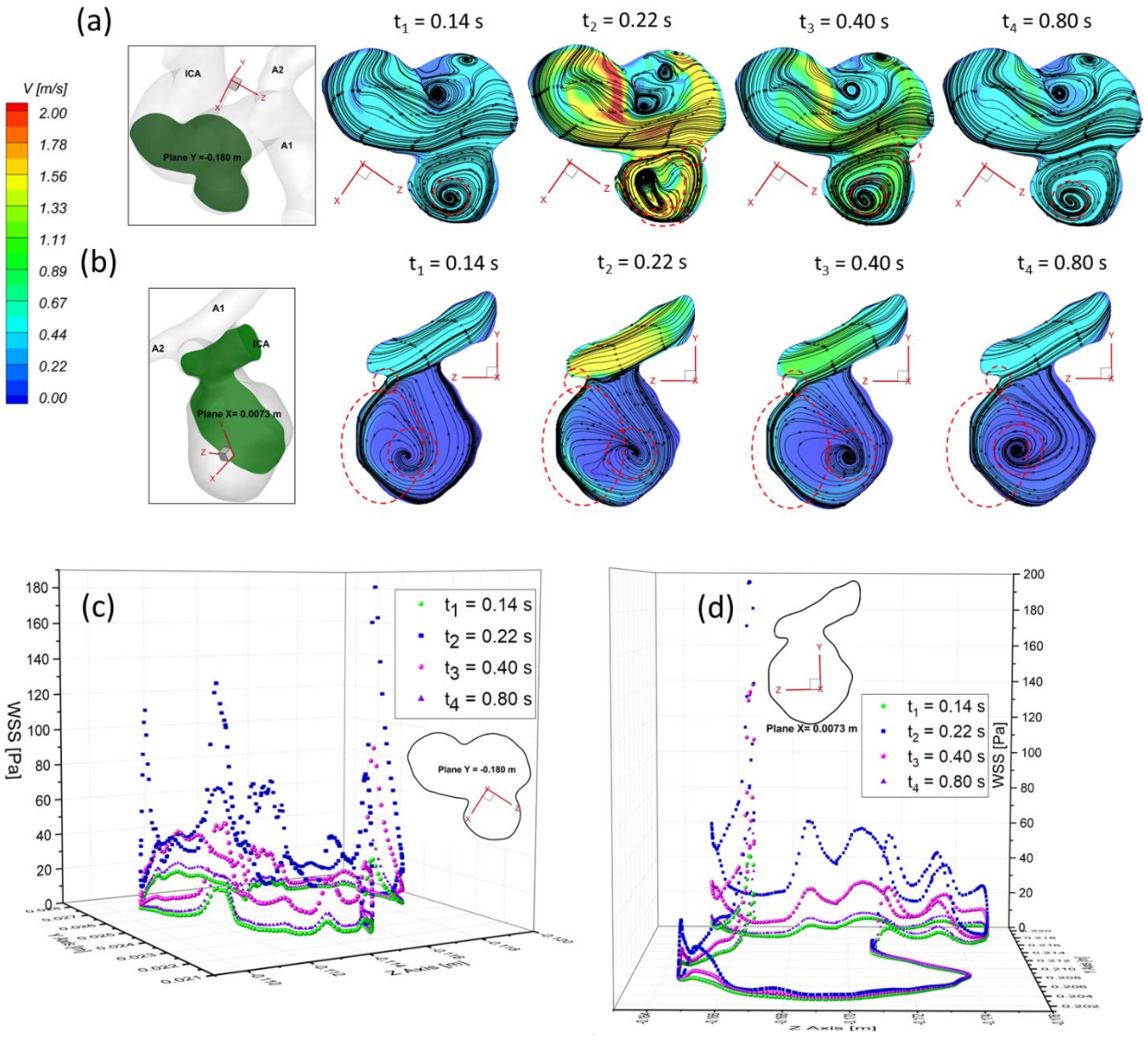

Figure 13. Comparisons of velocity profiles, flow streamlines, and WSS in selected planes of ICASA-1 and ICASA-2 models at selected time instants: (a) velocity profiles and streamlines in plane Y = -0.180 m of ICASA-1 model, (b) velocity profiles and streamlines in plane X = 0.0073 m of ICASA-2 model, (c) WSS distributions at the edge of plane Y = -0.180 m of ICASA-1 model, and (d) WSS distributions at the edge of plane X = 0.0205 m of ICASA-2.

To present the blood flow characteristics, the visualized velocity contours and flow streamlines in the plane of Y = -0.180 m in ICASA-1 model and in the plane of X = 0.007 m in ICASA-2 model have been presented in **Figs. 13 (a) & (b)** at the representative time instants (i.e., t_1 = 0.14 s, t_2 = 0.22 s, t_3 = 0.40 s, and t_4 = 0.80 s), separately. The CFD results show that the largest *WSS* is always located on the sac neck region (highlighted in **Figs. 13 (a) & (b)**), which is due to the strongest impingement by the blood stream onto the aneurysmal sac in both ICASA models, shown in **Figs. 13 (c) & (d)**. **Figures 13 (a) & (b)** manifest that the vortex plays a major role in the temporal and spatial distribution of the *WSS* on the sac wall, varying significantly along with the cardiac period. The unsteady vortex in

Preprints (www.preprints.org) | NOT PEER-REVIEWED | Posted: 30 May 2022 doi:10.20944/preprints202205.0400.v1

the aneurysmal sac increases velocity fluctuations, which not only leads to high WSS (e.g., see **Figs. 13 (c) & (d)**), but also causes high OSI, which has been discussed in **Section 3.1**. The findings in this study are consistent with the previous study that tracking the vortex formation and growth is a crucial step to analyze hemodynamic factors on the pathophysiology of the cerebral aneurysms [69]. Moreover, it is suggesting that the researchers should avoid using a non-pulsatile blood flow condition to conduct CFD simulations to investigate hemodynamic characteristics in cerebral aneurysms since it may cause significant differences between non-pulsatile and pulsatile conditions when predicting the flow characteristics in cerebral aneurysms.

4. CONCLUSIONS

In this study, the effects of pulsatile flow rates, shunt ratios in bifurcated distal arteries, and transient cardiac pulsatile blood flow on hemodynamic transport behaviors in the ICSASA -1 and ICSASA-2 models were investigated. Specifically, the main conclusions are summarized as follows:

- The pulsatile flow rate has a significant impact on hemodynamic characteristics in cerebral aneurysms. Larger pulsatile flow rates lead to higher WSS on the aneurysmal region, which may increase the risks to form small/secondary aneurysms. Although aneurysmal artery walls may suffer lower WSS under a lower pulsatile flow rate, the high OSI distributed in local regions may affect the growth and rupture of the cerebral aneurysms.
- The variances of shunt ratios in bifurcated distal arteries have no significant impacts on the hemodynamic behaviors in the aneurysmal sac because the distal bifurcated location is not close enough to the aneurysm sac in ICASA-2 model. We concede that more specific qualitative and quantitative investigations of the effects of bifurcated shunt ratios on flow characteristics in the aneurysmal sac using the patient-specific cerebral aneurysms are still needed.
- A higher PFR can contribute more to the pressure increase in the ICASA-1 dome due to the stronger impingement by the splitting blood stream, while the variances of PFR and shunt ratio in the bifurcated distal arteries have rare impacts on the dome of ICASA-2 model since only small part of blood stream will be redirected into the sac.
- The regions in the neck of the aneurysmal sac with higher WSS may lead to a high incidence of small/secondary aneurysm generation under all studied pulsatile flow rates and bifurcated shunt ratios. Also, some local luminal surfaces on the aneurysmal dome could have higher probability to enlarge/rupture given the evidence of relatively high OSI and low WSS features.
- During one pulse period, the blood flow at the systolic peak can influence the hemodynamic patterns (i.e., WSS and vortex) more than other time instants considerably. The slope of the increase of WSS is beyond the slope of the increase of the blood flow rate, and this phenomenon is more apparent under a smaller PFR.

Overall, the findings in this work can contribute to the intracranial aneurysm community's knowledge by providing better understanding of blood flow patterns in the aneurysmal sac and the effects of different patient-specific pulsatile flow rates and shunt ratios in bifurcated distal arteries.

5. LIMITATIONS AND FUTURE WORK

Blood is a non-Newtonian fluid with shear-thinning properties that was not considered in this study. Our following research will model the hemodynamic characteristics in the cerebral aneurysm model *in vitro* and *in silico*, integrating with the non-Newtonian properties of blood. This study did not simulate the arterial wall deformations coupled with the hemodynamic patterns explicitly. Accordingly, our long-term goal is to build a realistic *in-silico* model to conduct statistical analysis of the hemodynamic factors on the pathophysiology of the cerebral aneurysms (i.e., nearly 100 patient-specific aneurysmal models) using a two-way fluid-solid interaction (FSI) manner, i.e., the deformation effects between the cerebral artery wall and the realistic non-Newtonian blood.

ACKNOWLEDGEMENTS

This study is sponsored by National Heart, Lung, & Blood Institute with the award No. R44HL132664 and the Premier Health and Boonshoft School of Medicine Endowment Funding at Wright State University (WSU). The use of ANSYS software (Canonsburg, PA) as part of the ANSYS-WSU academic partnership agreement is gratefully acknowledged.

CONFLICT OF INTEREST

The authors have no conflicts to disclose.

REFERENCES

1. Cebral, J.R., et al., *Characterization of Cerebral Aneurysms for Assessing Risk of Rupture By Using Patient-Specific Computational Hemodynamics Models.* American Journal of Neuroradiology, 2005. **26**(10): p. 2550-2559.
2. Weir, B., *Unruptured intracranial aneurysms: a review.* Journal of Neurosurgery, 2002. **96**(1): p. 3-42.
3. Foutrakis, G.N., H. Yonas, and R.J. Sclabassi, *Saccular Aneurysm Formation in Curved and Bifurcating Arteries.* American Journal of Neuroradiology, 1999. **20**(7): p. 1309-1317.
4. Moossy, J., *Pathology of the Cerebral Blood Vessels.* Archives of Neurology, 1973. **28**(4): p. 284-284.
5. Jabbarli, R., et al., *Intracerebral Hematoma Due to Aneurysm Rupture: Are There Risk Factors Beyond Aneurysm Location?* Neurosurgery, 2016. **78**(6): p. 813-20.
6. Kaminogo, M., M. Yonekura, and S. Shibata, *Incidence and Outcome of Multiple Intracranial Aneurysms in a Defined Population.* Stroke, 2003. **34**(1): p. 16-21.
7. Linn, F.H.H., et al., *Incidence of Subarachnoid Hemorrhage.* Stroke, 1996. **27**(4): p. 625-629.
8. Winn, H.R., et al., *Prevalence of asymptomatic incidental aneurysms: review of 4568 arteriograms.* Journal of Neurosurgery, 2002. **96**(1): p. 43-49.
9. Byoun, H.S., et al., *Natural History of Unruptured Intracranial Aneurysms : A Retrospective Single Center Analysis.* Journal of Korean Neurosurgical Society, 2016. **59**(1): p. 11-16.
10. AANS, *Cerebral Aneurysm*. 2021, American Association of Neurological Surgeons.

11. ISOUIAI, *Unruptured Intracranial Aneurysms — Risk of Rupture and Risks of Surgical Intervention.* New England Journal of Medicine, 1998. **339**(24): p. 1725-1733.
12. Marosfoi, M., et al., *68 - Endovascular Treatment of Intracranial Aneurysms*, in *Stroke (Seventh Edition)*, J.C. Grotta, et al., Editors. 2022, Elsevier: Philadelphia. p. 985-1000.e4.
13. Cebral, J.R., et al., *Analysis of hemodynamics and wall mechanics at sites of cerebral aneurysm rupture.* Journal of NeuroInterventional Surgery, 2015. **7**(7): p. 530-536.
14. Shojima, M., et al., *Magnitude and Role of Wall Shear Stress on Cerebral Aneurysm.* Stroke, 2004. **35**(11): p. 2500-2505.
15. Papaioannou, T.G. and C. Stefanadis, *Vascular wall shear stress: basic principles and methods.* Hellenic J Cardiol, 2005. **46**(1): p. 9-15.
16. Meng, H., et al., *High WSS or Low WSS? Complex Interactions of Hemodynamics with Intracranial Aneurysm Initiation, Growth, and Rupture: Toward a Unifying Hypothesis.* American Journal of Neuroradiology, 2014. **35**(7): p. 1254-1262.
17. Sadasivan, C., et al., *Physical Factors Effecting Cerebral Aneurysm Pathophysiology.* Annals of Biomedical Engineering, 2013. **41**(7): p. 1347-1365.
18. Jeong, W. and K. Rhee, *Hemodynamics of Cerebral Aneurysms: Computational Analyses of Aneurysm Progress and Treatment.* Computational and Mathematical Methods in Medicine, 2012. **2012**: p. 782801.
19. Sheikh, M.A.A., A.S. Shuib, and M.H.H. Mohyi, *A review of hemodynamic parameters in cerebral aneurysm.* Interdisciplinary Neurosurgery, 2020. **22**: p. 100716.
20. Sforza, D.M., C.M. Putman, and J.R. Cebral, *Hemodynamics of Cerebral Aneurysms.* Annual Review of Fluid Mechanics, 2009. **41**(1): p. 91-107.
21. Yu, W., et al., *Effectiveness comparisons of drug therapies for postoperative aneurysmal subarachnoid hemorrhage patients: network meta-analysis and systematic review.* BMC Neurology, 2021. **21**(1): p. 294.
22. Nieuwkamp, D.J., et al., *Changes in case fatality of aneurysmal subarachnoid haemorrhage over time, according to age, sex, and region: a meta-analysis.* The Lancet Neurology, 2009. **8**(7): p. 635-642.
23. Nixon, A.M., M. Gunel, and B.E. Sumpio, *The critical role of hemodynamics in the development of cerebral vascular disease: A review.* Journal of Neurosurgery JNS, 2010. **112**(6): p. 1240-1253.
24. Aoki, T. and M. Nishimura, *The Development and the Use of Experimental Animal Models to Study the Underlying Mechanisms of CA Formation.* Journal of Biomedicine and Biotechnology, 2011. **2011**: p. 535921.
25. Fennell, V.S., et al., *Biology of Saccular Cerebral Aneurysms: A Review of Current Understanding and Future Directions.* Frontiers in Surgery, 2016. **3**(43).
26. Zarrinkoob, L., et al., *Blood Flow Distribution in Cerebral Arteries.* Journal of Cerebral Blood Flow & Metabolism, 2015. **35**(4): p. 648-654.

27. Enzmann, D.R., et al., *Blood flow in major cerebral arteries measured by phase-contrast cine MR.* American Journal of Neuroradiology, 1994. **15**(1): p. 123-129.
28. Sekhane, D. and K. Mansour, *Quantification Of the Effects Of the Inlet Waveform on Hemodynamics Inside Internal Carotid Arteries Using Computational Fluid Dynamics.* Sciences & Technology B, 2017(41): p. 27-36.
29. Sarrami-Foroushani, A., et al., *Effects of Variations of Flow and Heart Rate on Intra-Aneurysmal Hemodynamics in a Ruptured Internal Carotid Artery Aneurysm During Exercise.* Iran J Radiol, 2016. **13**(1): p. e18217.
30. Sunderland, K. and J. Jiang, *Multivariate analysis of hemodynamic parameters on intracranial aneurysm initiation of the internal carotid artery.* Medical Engineering & Physics, 2019. **74**: p. 129-136.
31. Valen-Sendstad, K., et al., *Estimation of Inlet Flow Rates for Image-Based Aneurysm CFD Models: Where and How to Begin?* Annals of Biomedical Engineering, 2015. **43**(6): p. 1422-1431.
32. Najafi, M., et al., *How patient-specific do internal carotid artery inflow rates need to be for computational fluid dynamics of cerebral aneurysms?* Journal of NeuroInterventional Surgery, 2021. **13**(5): p. 459-464.
33. Xiang, J., A.H. Siddiqui, and H. Meng, *The effect of inlet waveforms on computational hemodynamics of patient-specific intracranial aneurysms.* Journal of biomechanics, 2014. **47**(16): p. 3882-3890.
34. Rayz, V.L. and A.A. Cohen-Gadol, *Hemodynamics of Cerebral Aneurysms: Connecting Medical Imaging and Biomechanical Analysis.* Annual Review of Biomedical Engineering, 2020. **22**(1): p. 231-256.
35. Botti, L., et al., *Modeling hemodynamics in intracranial aneurysms: Comparing accuracy of CFD solvers based on finite element and finite volume schemes.* International Journal for Numerical Methods in Biomedical Engineering, 2018. **34**(9): p. e3111.
36. Alastruey, J., et al., *Modelling the circle of Willis to assess the effects of anatomical variations and occlusions on cerebral flows.* Journal of Biomechanics, 2007. **40**(8): p. 1794-1805.
37. Steinman, D.A., et al., *Image-Based Computational Simulation of Flow Dynamics in a Giant Intracranial Aneurysm.* American Journal of Neuroradiology, 2003. **24**(4): p. 559-566.
38. Kerber, C.W., S.G. Imbesi, and K. Knox, *Flow Dynamics in a Lethal Anterior Communicating Artery Aneurysm.* American Journal of Neuroradiology, 1999. **20**(10): p. 2000-2003.
39. Jou, L.-D., et al., *Computational Approach to Quantifying Hemodynamic Forces in Giant Cerebral Aneurysms.* American Journal of Neuroradiology, 2003. **24**(9): p. 1804-1810.

40. Hongo, K., et al., *Giant basilar bifurcation aneurysm presenting as a third ventricular mass with unilateral obstructive hydrocephalus: case report.* Journal of Clinical Neuroscience, 2001. **8**(1): p. 51-54.
41. Burleson, A.C., C.M. Strother, and V.T. Turitto, *Computer modeling of intracranial saccular and lateral aneurysms for the study of their hemodynamics.* Neurosurgery, 1995. **37**(4): p. 774-82; discussion 782-4.
42. Sforza, D.M., C.M. Putman, and J.R. Cebral, *Hemodynamics of Cerebral Aneurysms.* Annual review of fluid mechanics, 2009. **41**: p. 91-107.
43. Soldozy, S., et al., *The biophysical role of hemodynamics in the pathogenesis of cerebral aneurysm formation and rupture.* Neurosurgical Focus FOC, 2019. **47**(1): p. E11.
44. Yu, H., et al., *Numerical studies of hemodynamic alterations in pre- and post-stenting cerebral aneurysms using a multiscale modeling.* International Journal for Numerical Methods in Biomedical Engineering, 2019. **35**(11): p. e3256.
45. Yang, Z., et al., *Computational fluid dynamics simulation of intracranial aneurysms – comparing size and shape.* Journal of Coastal Life Medicine, 2015. **3**(3): p. 245-252.
46. Ford, M.D., et al., *PIV-Measured Versus CFD-Predicted Flow Dynamics in Anatomically Realistic Cerebral Aneurysm Models.* Journal of Biomechanical Engineering, 2008. **130**(2).
47. Raschi, M., et al., *CFD and PIV analysis of hemodynamics in a growing intracranial aneurysm.* International Journal for Numerical Methods in Biomedical Engineering, 2012. **28**(2): p. 214-228.
48. Sun, Q., A. Groth, and T. Aach, *Comprehensive validation of computational fluid dynamics simulations of in-vivo blood flow in patient-specific cerebral aneurysms.* Medical Physics, 2012. **39**(2): p. 742-754.
49. Brindise, M.C., et al., *Multi-modality cerebral aneurysm haemodynamic analysis: in vivo 4D flow MRI, in vitro volumetric particle velocimetry and in silico computational fluid dynamics.* Journal of The Royal Society Interface, 2019. **16**(158): p. 20190465.
50. Roloff, C., et al., *Comparison of intracranial aneurysm flow quantification techniques: standard PIV vs stereoscopic PIV vs tomographic PIV vs phase-contrast MRI vs CFD.* Journal of NeuroInterventional Surgery, 2019. **11**(3): p. 275-282.
51. Li, Y., et al., *A pilot validation of CFD model results against PIV observations of haemodynamics in intracranial aneurysms treated with flow-diverting stents.* Journal of Biomechanics, 2020. **100**: p. 109590.
52. Wüstenhagen, C., et al., *CFD validation using in-vitro MRI velocity data – Methods for data matching and CFD error quantification.* Computers in Biology and Medicine, 2021. **131**: p. 104230.

53. Himburg, H.A., et al., *Spatial comparison between wall shear stress measures and porcine arterial endothelial permeability.* Am J Physiol Heart Circ Physiol, 2004. **286**(5): p. H1916-22.
54. Sandvei, M.S., et al., *Risk Factors for Aneurysmal Subarachnoid Hemorrhage in a Prospective Population Study.* Stroke, 2009. **40**(6): p. 1958-1962.
55. Tada, Y., et al., *Roles of Hypertension in the Rupture of Intracranial Aneurysms.* Stroke, 2014. **45**(2): p. 579-586.
56. Chalouhi, N., B.L. Hoh, and D. Hasan, *Review of Cerebral Aneurysm Formation, Growth, and Rupture.* Stroke, 2013. **44**(12): p. 3613-3622.
57. Yu, H., et al., *A multiscale computational modeling for cerebral blood flow with aneurysms and/or stenoses.* International Journal for Numerical Methods in Biomedical Engineering, 2018. **34**(10): p. e3127.
58. Klötzsch, C., O. Popescu, and P. Berlit, *Assessment of the Posterior Communicating Artery by Transcranial Color-Coded Duplex Sonography.* Stroke, 1996. **27**(3): p. 486-489.
59. Tanaka, H., et al., *Relationship between variations in the circle of Willis and flow rates in internal carotid and basilar arteries determined by means of magnetic resonance imaging with semiautomated lumen segmentation: reference data from 125 healthy volunteers.* AJNR Am J Neuroradiol, 2006. **27**(8): p. 1770-5.
60. Metaxa, E., et al., *Characterization of Critical Hemodynamics Contributing to Aneurysmal Remodeling at the Basilar Terminus in a Rabbit Model.* Stroke, 2010. **41**(8): p. 1774-1782.
61. Isaksen, J.G., et al., *Determination of Wall Tension in Cerebral Artery Aneurysms by Numerical Simulation.* Stroke, 2008. **39**(12): p. 3172-3178.
62. Lu, D. and G.S. Kassab, *Role of shear stress and stretch in vascular mechanobiology.* Journal of the Royal Society, Interface, 2011. **8**(63): p. 1379-1385.
63. Wegener, P.P., *What Makes Airplanes Fly?* 1 ed. 1991, NY: Springer.
64. Zhang, Y., et al., *Low wall shear stress is associated with the rupture of intracranial aneurysm with known rupture point: case report and literature review.* BMC Neurology, 2016. **16**(1): p. 231.
65. Malek, A.M., S.L. Alper, and S. Izumo, *Hemodynamic shear stress and its role in atherosclerosis.* Jama, 1999. **282**(21): p. 2035-42.
66. Nixon, A.M., M. Gunel, and B.E. Sumpio, *The critical role of hemodynamics in the development of cerebral vascular disease.* J Neurosurg, 2010. **112**(6): p. 1240-53.
67. Yen, W., et al., *Endothelial Surface Glycocalyx Can Regulate Flow-Induced Nitric Oxide Production in Microvessels In Vivo.* PLOS ONE, 2015. **10**(1): p. e0117133.
68. Joyner, M.J. and D.P. Casey, *Regulation of increased blood flow (hyperemia) to muscles during exercise: a hierarchy of competing physiological needs.* Physiological reviews, 2015. **95**(2): p. 549-601.

 doi:10.20944/preprints202205.0400.v1

69. Bauer, A., et al., *Analysis of the wall shear stress in a generic aneurysm under pulsating and transitional flow conditions.* Experiments in Fluids, 2020. **61**(2): p. 59.